

# Seismic Acoustic Impedance Inversion via Optimization-Inspired Semisupervised Deep Learning

Hongling Chen<sup>1</sup>, Jinghuai Gao<sup>1</sup>, Wei Zhang<sup>1</sup>, and Ping Yang

**Abstract**—Seismic acoustic impedance inversion (SAII) aims at recovering the subsurface impedance to achieve lithology interpretation. However, its ill-posedness and nonlinearity pose a great challenge to find an optimal solution. Regularization is an effective method to solve SAI by imposing prior information, but it suffers from high computational complexity and limited inversion performance. To mitigate the above limitations, we propose an optimization-inspired semisupervised deep learning SAI approach that incorporates the advantages between the model-driven optimization algorithm and the data-driven deep learning method. Specifically, it is implemented by parameterizing the alternating iterative method (AIM) by splitting it into two parts where the convolutional neural networks are adopted to learn the regularization terms and a nonlinear mapping and thus called the proposed network as AIM-SAIINet. The proposed method can not only simultaneously invert the seismic wavelet and impedance but also obtain high-resolution data as an intermediate product to facilitate the training of AIM-SAIINet and enhance the inversion accuracy. In addition, we introduce a joint semisupervised training scheme in which the network is first jointly pretrained in a supervised manner using the synthetic training data to provide good initial values, and then, a semisupervised training scheme is adopted to fine-tune it using few labeled data pairs to achieve high inversion accuracy. The synthetic and field data examples are conducted to validate the effectiveness of AIM-SAIINet, which achieves higher inversion accuracy at a fast computational speed compared with the traditional methods.

**Index Terms**—Deep learning, impedance inversion, seismic inversion.

## I. INTRODUCTION

SEISMIC acoustic impedance inversion (SAII), which builds a bridge between seismic data and quantitative geology, plays a crucial role in seismic exploration. It can infer acoustic impedance from poststack seismic data, which is conducive to predicting stratigraphic lithology parameters [1],

e.g., porosity or sand/shale fraction, for achieving lithologic reservoir exploration. Up to now, various SAI methods are proposed to obtain high accuracy acoustic impedance. In general, there are two techniques used in impedance inversion, i.e., model- and data-driven methods.

Model-driven method here refers to the method using a loss function constructed based on the objective, physical mechanism, and domain knowledge for impedance inversion [2]. It is a commonly used inversion scheme, usually including two-step inversion and direct inversion. The two-step inversion method includes two sequential inversion steps [3], [4], i.e., the first step indicates reflectivity inversion and the second step is to map this reflectivity into acoustic impedance. The reflectivity inversion can mitigate the influence of the seismic wavelet to provide accurate interface information. When the seismic wavelet is known, the reflectivity inversion is a nonblind problem [5]–[8]. However, the seismic wavelet is usually unknown, and thus, blind reflectivity inversion methods are commonly adopted to simultaneously estimate reflectivity and wavelet [9]–[12]. The inverted reflectivity can be transformed into acoustic impedance by the standard recursion formulas [13], [14]. However, the above schemes are affected by noise, poor amplitude recovery, and the band-limited nature of seismic data. Except for the recursion inversion, the regularization can be adopted to turn the estimated reflectivity into impedance by adding some prior constraints, e.g., the research of [4], which can improve the inversion accuracy. Generally, the two-step inversion scheme generates irreversible losses because the impedance inversion procedure is dependent on the result of the estimated reflectivity.

Another effective impedance inversion method is direct inversion. Direct inversion can directly achieve impedance from seismic data via linear or nonlinear inversion methods. One of the linear strategies is to simplify the forward model using a logarithm relationship. There is a requirement that the absolute value of the reflectivity is less than 0.3 in this case [15]. This linear inversion problem is mathematically ill-posed due to the singularity of the forward operator. In general, it can be alleviated by incorporating some prior information about impedance [16]–[18], e.g., smoothness or sparsity. The above regularization method is attractive because of its high inversion accuracy; however, the approximated forward model is valid for only small reflectivity, the computational cost is high, and the predetermined parameters are sensitive. Another linear strategy is to use the generalized linear inversion

Manuscript received May 18, 2021; revised July 19, 2021; accepted August 17, 2021. Date of publication September 3, 2021; date of current version January 31, 2022. This work was supported in part by the National Key R&D Program of China under Grant 2018YFC0603501, Grant 2020YFA0713403, and Grant 2020YFA0713400; and in part by the Fundamental Research Funds for the Central Universities under Grant xzy022020053. (Corresponding author: Jinghuai Gao.)

Hongling Chen, Jinghuai Gao, and Wei Zhang are with the School of Information and Communications Engineering, Faculty of Electronic and Information Engineering, Xi'an Jiaotong University, Xi'an 710049, China, and also with the National Engineering Laboratory for Offshore Oil Exploration, Xi'an 710049, China (e-mail: 859311743@qq.com; jhgao@xjtu.edu.cn; zhangwei\_geo@sina.com).

Ping Yang is with BGP Inc., China National Petroleum Corporation, Zhuozhou 072751, China (e-mail: 603500974@qq.com).

Digital Object Identifier 10.1109/TGRS.2021.3107257

1558-0644 © 2021 IEEE. Personal use is permitted, but republication/redistribution requires IEEE permission.

See <https://www.ieee.org/publications/rights/index.html> for more information.

technique based on a Taylor series expansion of the forward model to solve the nonlinear inverse problem [19], [20] in the case of the nonlinear forward model. Though the generalized linear inversion is robust compared to the Gauss–Newton method, it requires an accurate initial model to yield a high accuracy impedance. The global optimization method is an alternative [21], [22], and it can search for a global minimum of the loss function without the requirements of an accurate initial model and linearizing the inverse problem. However, global optimization methods rarely work for large-dimensional problems because they are computationally intensive and converge slowly.

Recently, deep learning, which is a data-driven method, is gaining popularity in the geoscientific community, and it has been successfully applied to solve geophysical problems, e.g., seismic interpretation [23], [24] and processing [25]. Deep learning has a great learning ability to learn a nonlinear relation and apply it to solve various seismic inverse problems. To our knowledge, there are two kinds of deep learning inverse methods, i.e., data- and model-driven deep learning methods. Data-driven deep learning method indicates that a deep neural network is utilized to learn a target mapping without incorporating any physical knowledge [26], [27]. For instance, Das *et al.* [28] proposed a convolutional neural network without combining any prior information to implement the impedance inversion and estimated the posterior distribution to quantify the uncertainty. Wang *et al.* [29] proposed a closed-loop convolutional neural network to invert the acoustic impedance, which can be treated as an autoencoder to model forward and inversion processes simultaneously. Model-driven deep learning method here refers that the domain knowledge and mathematical models are incorporated with deep neural networks to solve inverse problems [30]–[32]. For instance, our work in [33] proposed an optimization-inspired deep learning blind high-resolution inversion method by unrolling the alternating iterative optimization algorithm to build a novel deep neural network incorporating model prior information. Model-driven deep learning methods, which have achieved great success in image processing and imaging [34], are becoming attractive, and they combine the advantages of data-driven deep learning and model-driven optimization methods [2]. On one hand, deep neural network has a great learning ability, and it can be used to learn prior information or regularizers to improve the performance and computational efficiency of the model-driven optimization methods. On the other hand, model-driven optimization method has determinacy and theoretical soundness, and it can inspire us to design novel deep neural network structures and integrate prior information obtained from mathematical models to increase the interpretation of deep neural networks and improve their performance.

Based on the advantages of model-driven deep learning methods, we provide an optimization-inspired semisupervised deep learning impedance inversion method, called AIM-SAIINet. In this work, we extend our previous work [33] to adapt to impedance inversion. Here, we focus on implementing blind acoustic impedance inversion; therefore, the alternating iterative method (AIM) is an efficient

optimization algorithm. We parameterize AIM by combining deep neural networks to improve the inversion accuracy and computational efficiency of AIM. The main contributions of this work can be summarized as follows.

- 1) The proposed AIM-SAIINet incorporates the model- and data-driven deep learning methods to build a joint deep neural network to perform the blind nonlinear acoustic impedance inversion for simultaneously achieving seismic wavelet and impedance. Compared with regularization, the proposed network can avoid the pre-determination of all unknown terms, e.g., regularization terms, by applying more easily operated deep neural networks.
- 2) To facilitate the training and obtain high inversion accuracy, we establish a joint loss function to obtain an intermediate product (high-resolution data) in addition to seismic wavelet and impedance. In addition, a joint semisupervised training scheme is introduced to make the proposed AIM-SAIINet adapt to few labeled data, before which we adopt the synthetic data to train it in a supervised manner to provide good initial values.
- 3) We achieve better impedance inversion results using AIM-SAIINet than those using the existing state-of-the-art methods in the synthetic and field data examples. Especially, the computational efficiency is higher.

## II. NONLINEAR SEISMIC ACOUSTIC IMPEDANCE INVERSION FRAMEWORK

### A. Nonlinear Impedance Inversion Framework

Based on the Robinson convolution model, the seismic trace can be modeled as

$$\mathbf{y} = \mathbf{W}\mathbf{r} = \mathbf{W}D(\mathbf{z}) \quad (1)$$

where  $\mathbf{y} \in \mathbf{R}^n$  is an observed seismic trace,  $\mathbf{W} \in \mathbf{R}^{n \times n}$  is a Toeplitz matrix consisting of seismic wavelet  $\mathbf{w}$ , and  $\mathbf{r} \in \mathbf{R}^n$  denotes the reflectivity. The vector  $\mathbf{z} \in \mathbf{R}^{n+1}$  is the seismic acoustic impedance, and the nonlinear operator  $D$  represents the relation between the reflectivity and the acoustic impedance. The nonlinear relation  $D(\mathbf{z})$  is represented as

$$\mathbf{r} = D(\mathbf{z}) = \sum_{i=0}^{n-1} \frac{\mathbf{z}_{i+1} - \mathbf{z}_i}{\mathbf{z}_{i+1} + \mathbf{z}_i} \delta_i \quad (2)$$

where  $n$  is the total time sampling number,  $i$  is the  $i$ th time point, and  $\delta$  is the impulse function. The SAIIN framework, which aims at finding the optimal solution to minimize the loss function between the observed data and the calculated data, can be represented as the following form:

$$\hat{\mathbf{z}} = \arg \min_{\mathbf{z}} \frac{1}{2} \|\mathbf{y} - \mathbf{W}D(\mathbf{z})\|_2^2 \quad (3)$$

where  $\hat{\mathbf{z}}$  is the optimal solution. Here, the  $L^2$ -norm-based misfit function is adopted.

The inverse problem (3) is ill-posed because of the band-limited seismic wavelet, the noise, and the nonlinearity of the forward operator. It means that there is no unique solution. Furthermore, the seismic wavelet is unknown in the real application, i.e., the matrix  $\mathbf{W}$  needs to be estimated.

Considering the estimation of the seismic wavelet, the regularization method is adopted, and then, the objective function is described as

$$\hat{\mathbf{z}}, \hat{\mathbf{w}} = \arg \min_{\mathbf{z}, \mathbf{w}} \frac{1}{2} \|\mathbf{y} - \mathbf{w} * D(\mathbf{z})\|_2^2 + \lambda \Psi(\mathbf{z}) + \beta \Phi(\mathbf{w}) \quad (4)$$

where  $\hat{\mathbf{w}}$  denotes the estimated wavelet and  $*$  denotes the convolution symbol.  $\Psi$  and  $\Phi$  represent the regularization functions corresponding to variables  $\mathbf{z}$  and  $\mathbf{w}$ , respectively, and they impose some prior information to model parameters to make the inverse problem well-conditioned. Generally,  $\Psi$  is set as a smooth or sparsity regularization, e.g., total variation (TV), and  $\Phi$  is set as a smooth or sparsity regularization or both, e.g.,  $L_2$ -norm or fused lasso.  $\lambda$  and  $\beta$  are the regularization parameters.

### B. AIM Solvers

To solve the optimization problem (4), we can rewrite it as the following equation by introducing an auxiliary variable  $\tilde{\mathbf{r}}$ :

$$\min_{\mathbf{z}, \mathbf{w}, \tilde{\mathbf{r}}} \frac{1}{2} \|\mathbf{y} - \mathbf{w} * \tilde{\mathbf{r}}\|_2^2 + \lambda \Psi(\mathbf{z}) + \beta \Phi(\mathbf{w}) \quad \text{s.t. } \tilde{\mathbf{r}} = D(\mathbf{z}) \quad (5)$$

where the auxiliary variable  $\tilde{\mathbf{r}}$  has a special physical meaning, i.e., it is equal to reflectivity in the case of the accurate impedance according to (2). Here, we add a constraint about  $\tilde{\mathbf{r}}$  to make it approximate accurate reflectivity and thus promote the accurate inversion of the impedance. The Lagrangian associated with (5) is

$$\min_{\mathbf{z}, \mathbf{w}, \tilde{\mathbf{r}}} \frac{1}{2} \|\mathbf{y} - \mathbf{w} * \tilde{\mathbf{r}}\|_2^2 + \lambda \Psi(\mathbf{z}) + \beta \Phi(\mathbf{w}) + \mu \|\tilde{\mathbf{r}} - D(\mathbf{z})\|_2^2 + \alpha \Lambda(\tilde{\mathbf{r}}) \quad (6)$$

where  $\mu$  denotes a penalty parameter,  $\Lambda$  is the regularization function corresponding to  $\tilde{\mathbf{r}}$ , and  $\alpha$  denotes the corresponding regularization parameter. This inverse problem can be optimized by splitting it into the following three subproblems:

$$\min_{\tilde{\mathbf{r}}} \frac{1}{2} \|\mathbf{y} - \mathbf{w} * \tilde{\mathbf{r}}\|_2^2 + \mu \|\tilde{\mathbf{r}} - D(\mathbf{z})\|_2^2 + \alpha \Lambda(\tilde{\mathbf{r}}) \quad (7a)$$

$$\min_{\mathbf{w}} \frac{1}{2} \|\mathbf{y} - \mathbf{w} * \tilde{\mathbf{r}}\|_2^2 + \beta \Phi(\mathbf{w}) \quad (7b)$$

$$\min_{\mathbf{z}} \lambda \Psi(\mathbf{z}) + \mu' \|\tilde{\mathbf{r}} - D(\mathbf{z})\|_2^2 \quad (7c)$$

where we set  $\mu'$  and  $\mu$  to different values to increase the flexibility. For solving the above optimization problem, AIM is an efficient algorithm. Specifically, when the impedance  $\mathbf{z}$  is fixed,  $\mathbf{w}$  and  $\tilde{\mathbf{r}}$  can be inverted by solving (7a) and (7b) alternately. Then,  $\tilde{\mathbf{r}}$  and  $\mathbf{z}$  can be updated by optimizing (7a) and (7c) in the case of fixing  $\mathbf{w}$ . Finally, these three variables can be obtained by interactive iterations.

However, all unknown items need to be predetermined, such as regularization terms and sensitive parameters, for obtaining the above solutions. It is a challenging task to determine them optimally to obtain accurate inversion results. In addition, the update gradient requires one to calculate the gradients of the nonlinear forward operator and regularization terms (need to be predetermined), which increases the computational complexity and easily makes the solution fall into local minima.

To improve the computational efficiency and inversion accuracy, we introduce a semisupervised deep neural network in the following to learn all unknown terms (i.e., regularization terms, sensitive parameters, and gradients) and apply the error backpropagation algorithm to update network parameters to make the target variable  $\mathbf{z}$  optimal.

### III. SEMISUPERVISED DEEP LEARNING ACOUSTIC IMPEDANCE INVERSION

Introducing the deep neural network into the optimization algorithm is an effective approach to address the above limitations of AIM, and it has a heuristic effect on the establishment of new deep neural networks. Here, we follow this idea to set  $\mu = 0$  in (7) to build a plug-and-play deep neural network structure called AIM-SAIHNet for performing the impedance inversion. It can be phrased as the problem of finding a pseudoinverse operator  $\mathcal{T}_{\Theta}^{\dagger}$

$$\mathcal{T}_{\Theta}^{\dagger}(\mathbf{y}) = \mathcal{B}_{\Theta''}^{\dagger} \circ \mathcal{C}_{\Theta'}^{\dagger}(\mathbf{y}, \tilde{\mathbf{r}}) \approx \mathbf{z} \quad (8)$$

where the pseudoinversion operator  $\mathcal{T}_{\Theta}^{\dagger}$  is a learning operator with parameter set  $\Theta$ , and it maps the observed seismic data  $\mathbf{y}$  into the acoustic impedance approximating to the true impedance  $\mathbf{z}$ . Here, we use two joint pseudoinverse operators  $\mathcal{C}_{\Theta'}^{\dagger}$  and  $\mathcal{B}_{\Theta''}^{\dagger}$  with parameters  $\Theta'$  and  $\Theta''$  to replace  $\mathcal{T}_{\Theta}^{\dagger}$ , and the parameter set  $\Theta = \Theta' \cup \Theta''$ .  $\mathcal{C}_{\Theta'}^{\dagger}(\mathbf{a}, \mathbf{b})$  shows that the input is  $\mathbf{a}$  and the output is  $\mathbf{b}$ , and it denotes a learning operator that maps the observed seismic data into the seismic wavelet and auxiliary high-resolution data by solving (7a) and (7b), and  $\mathcal{B}_{\Theta''}^{\dagger}$  denotes a learning component that maps the auxiliary high-resolution inversion data into the impedance by solving (7c). A key element in problem (8) is to parameterize the sets of these two operators by  $\Theta'$  and  $\Theta''$  within a suitable parameter space. The following introduces the parameterized AIM. Note that we filter the full-band reflectivity to obtain the limited-band reflectivity, which is similar to our work in [33]. Therefore, we call reflectivity high-resolution data. Moreover, different from the conventional two-step inversion, a joint training strategy, which can transmit the impedance information to promote the updates of wavelet and high-resolution result by the error backpropagation algorithm, is adopted to alleviate the intermediate loss.

#### A. Parameterized AIM

In the case of  $\mu = 0$ , we split (7) into two learning tasks, i.e.,  $\mathcal{C}_{\Theta'}^{\dagger}$  and  $\mathcal{B}_{\Theta''}^{\dagger}$ . Based on our previous work [33], we have built a model-driven deep neural network to learn  $\mathcal{C}_{\Theta'}^{\dagger}$  for targeting high-resolution data. Here, we simplify and tune it to adapt to an impedance inversion problem, i.e., the inverted high-resolution data are treated as auxiliary data to promote the impedance inversion. The learning solutions of (7a) and (7b) are represented as

$$\mathbf{x}_{\tilde{\mathbf{r}}}^k = \mathcal{F}^{-1} \left( \frac{[\mathcal{F}(\mathbf{w}^{k-1})]^* \odot \mathcal{F}(\mathbf{y}) + \zeta_1^k \mathcal{F}(\tilde{\mathbf{r}}^{k-1})}{[\mathcal{F}(\mathbf{w}^{k-1})]^* \odot \mathcal{F}(\mathbf{w}^{k-1}) + \zeta_1^k} \right) \quad (9a)$$

$$\tilde{\mathbf{r}}^k = \Gamma_{\Theta_g}((\tilde{\mathbf{r}}^{k-1}, \mathbf{x}_{\tilde{\mathbf{r}}}^k), \mathbf{x}_{\tilde{\mathbf{r}}}^k) = \text{prox}_{\zeta_1^k g}(\mathbf{x}_{\tilde{\mathbf{r}}}^k), \quad (9b)$$

$$\mathbf{x}_{\mathbf{w}}^k = \mathcal{F}^{-1} \left( \frac{[\mathcal{F}(\tilde{\mathbf{r}}^k)]^* \odot \mathcal{F}(\mathbf{y}) + \zeta_2^k \mathcal{F}(\mathbf{w}^{k-1})}{[\mathcal{F}(\tilde{\mathbf{r}}^k)]^* \odot \mathcal{F}(\tilde{\mathbf{r}}^k) + \zeta_2^k} \right) \quad (9c)$$

$$\mathbf{w}^k = \Gamma_{\Theta_f}((\mathbf{w}^{k-1}, \mathbf{x}_{\mathbf{w}}^k), \mathbf{w}^{k-1}) = \text{prox}_{\zeta_2^k f}(\mathbf{x}_{\mathbf{w}}^k) \quad (9d)$$



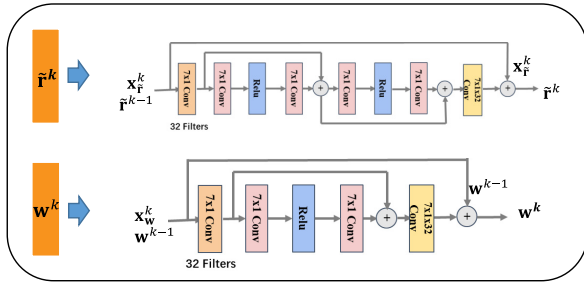


Fig. 1. Convolutional neural networks are used to learn the proximal operators corresponding to (9b) and (9d). The first network includes two residual convolutional blocks, and the second includes one residual convolutional block, where each residual convolutional block consists of two “Conv” (convolution) layers and one “Relu” (activation) layer. Both have a large skip connection to construct a network to learn update gradient. There are 32 filters with a kernel size of  $7 \times 1$  for each layer, except for the last layer that has only one filter with a kernel size of  $7 \times 1 \times 32$ .

where the derivation of (9a)–(9d) can be reviewed in Appendix A where the half-quadratic splitting (HQS) algorithm is adopted to solve (7a) and (7b).  $k$  denotes the  $k$ th iteration,  $\mathbf{x}_f^k$  and  $\mathbf{x}_w^k$  denote the introduced auxiliary variables at the  $k$ th iteration,  $\mathcal{F}$  and  $\mathcal{F}^{-1}$  denote the Fourier transform and its inverse transform, respectively,  $*$  denotes the conjugate,  $\odot$  denotes the Hadamard (elementwise) product operator, and  $\zeta_1$  and  $\zeta_2$  denote the penalty parameters treated as weights of the deep neural network to learn from training data.  $\text{prox}_{\zeta_1^k g}$  and  $\text{prox}_{\zeta_2^k f}$  represent the proximal operators to, respectively, map the auxiliary variables  $\mathbf{x}_f^k$  and  $\mathbf{x}_w^k$  to high-resolution data  $\tilde{\mathbf{r}}^k$  and seismic wavelet  $\mathbf{w}^k$  at the  $k$ th iteration, where  $g = \alpha \Lambda(\tilde{\mathbf{r}})$  and  $f = \beta \Phi(\mathbf{w})$ .  $\Gamma_{\Theta_g^k}$  and  $\Gamma_{\Theta_f^k}$  denote the learning operators at the  $k$ th iteration with parameters  $\Theta_g^k$  and  $\Theta_f^k$ , and they are used to replace the above proximal operators by building residual convolutional neural networks to learn update gradient operator  $\Delta$ . Therefore, we represent  $\Gamma_{\Theta_g^k}((\tilde{\mathbf{r}}^{k-1}, \mathbf{x}_f^k), \mathbf{x}_f^k) = \mathbf{x}_f^k + \Delta_{\Theta_g^k}(\tilde{\mathbf{r}}^{k-1}, \mathbf{x}_f^k)$  with inputs  $\tilde{\mathbf{r}}^{k-1}$  and  $\mathbf{x}_f^k$ , where  $\Delta_{\Theta_g^k}$  is a learning update gradient operator in  $\Gamma_{\Theta_g^k}$ . Different from our previous work in [33], we revise  $\Gamma_{\Theta_f^k}((\mathbf{w}^{k-1}, \mathbf{x}_w^k), \mathbf{x}_w^k)$  as  $\Gamma_{\Theta_f^k}((\mathbf{w}^{k-1}, \mathbf{x}_w^k), \mathbf{w}^{k-1}) = \mathbf{w}^{k-1} + \Delta_{\Theta_f^k}(\mathbf{w}^{k-1}, \mathbf{x}_w^k)$  with inputs  $\mathbf{w}^{k-1}$  and  $\mathbf{x}_w^k$  to make the training procedure stable, where  $\Delta_{\Theta_f^k}$  is a learning update gradient operator in  $\Gamma_{\Theta_f^k}$ . The main reason is that the seismic wavelet waveform is simple and the initial value  $\mathbf{w}^0$  approximates to accurate value; therefore, updating the gradient based on the wavelet of the last iteration can increase the convergence of AIM-SAINet. Fig. 1 shows the convolutional neural network corresponding to learning operators  $\Gamma_{\Theta_g^k}$  and  $\Gamma_{\Theta_f^k}$ . The left section in Fig. 2 shows the complete end-to-end model-driven deep neural network that is built by unrolling (9a)–(9d) into three stages ( $N_t = 3$ ). Here, we remove the additional two stages related to the high-resolution data in [33] because the high-resolution data are auxiliary data without requiring very high inversion accuracy.

For (7c), we use a deep neural network to learn  $\mathcal{B}_{\Theta''}^\dagger$  to map the auxiliary high-resolution data obtained from  $\mathcal{C}_{\Theta'}^\dagger$  into

the impedance in the case of given low-frequency impedance. In such a situation, (7c) has the following solution form:

$$\hat{\mathbf{z}} = \mathcal{B}_{\Theta''}^\dagger(\tilde{\mathbf{r}}) + \mathbf{z}_l \quad (10)$$

where  $\mathbf{z}_l$  denotes the given low-frequency impedance. The low-frequency background information is very important, and its accuracy directly affects the inversion accuracy of the impedance. Generally, the low-frequency component can be obtained by filtering the well logs; however, it lacks a lateral component and thus does not apply to the complex subsurface structures. Another effective way is the full-waveform inversion [35], [36], which can obtain a more credible low-frequency component compared to that obtained by filtering from well logs. Here, how to obtain accurate low-frequency impedance has exceeded the scope of our research. We assume that the low-frequency impedance is known. For (10), any deep neural networks can be applied to learn  $\mathcal{B}_{\Theta''}^\dagger$ . Here, we adopt the U-Net architecture because it takes full use of the advantages of multiscale information and has been applied to seismic inversion with good results, for instance, [32] used U-Net to reconstruct low and high wavenumber components of subsurface velocity by incorporating prior information. The right section in Fig. 2 shows the modified U-Net architecture. The original U-Net architecture is designed for biomedical image segmentation [37]. Based on our impedance inversion task, the input data are a 1-D seismic trace; therefore, we modify 2-D U-Net as 1-D U-Net, and there are  $3 \times 1$  convolution,  $2 \times 1$  max-pooling operation, and  $2 \times 1$  upconvolution. In addition, the number of channels is consistent with that in [37].

Based on the above substitutions, the parameterized AIM is expressed as follows:

$$\tilde{\mathbf{r}}, \hat{\mathbf{w}} = \mathcal{C}_{\Theta'}^\dagger(\mathbf{y}) \quad (11a)$$

$$\hat{\mathbf{z}} = \mathcal{B}_{\Theta''}^\dagger(\tilde{\mathbf{r}}) + \mathbf{z}_l. \quad (11b)$$

Fig. 2 shows the parameterized AIM, i.e., a joint deep neural network AIM-SAINet, which consists of two parts. The first part is the left network in the black box with nonshared parameters, called AIM-SAINet-I. The second part is the U-Net, called AIM-SAINet-II, where the output of AIM-SAINet-I is treated as the input of AIM-SAINet-II. Though variable  $\mathbf{z}$  is not used to update variables  $\tilde{\mathbf{r}}$  and  $\mathbf{w}$  in the feedforward learning process, it can be used to update the parameters of AIM-SAINet-I by an error backpropagation algorithm and thus affects the inversions of  $\tilde{\mathbf{r}}$  and  $\mathbf{w}$ . The following gradient formula can show this:

$$\frac{\partial E}{\partial \Theta'} = \frac{\partial E}{\partial \mathbf{z}} \frac{\partial \mathbf{z}}{\partial \Theta''} \frac{\partial \Theta''}{\partial \tilde{\mathbf{r}}} \frac{\partial \tilde{\mathbf{r}}}{\partial \Theta'} \quad (12)$$

where  $E$  is the loss function, which is built in Section III-B.

### B. Optimization

According to (11), parameters in AIM-SAINet include  $\Theta = \Theta' \cup \Theta''$ , where  $\Theta'$  contains  $(\zeta_1^k, \zeta_2^k, \Theta_g^k, \Theta_f^k)_{k=1}^{N_t}$  and  $N_t$  is the stage number. The optimization of  $\Theta$  includes three approaches, i.e., sequential approach, end-to-end approach,

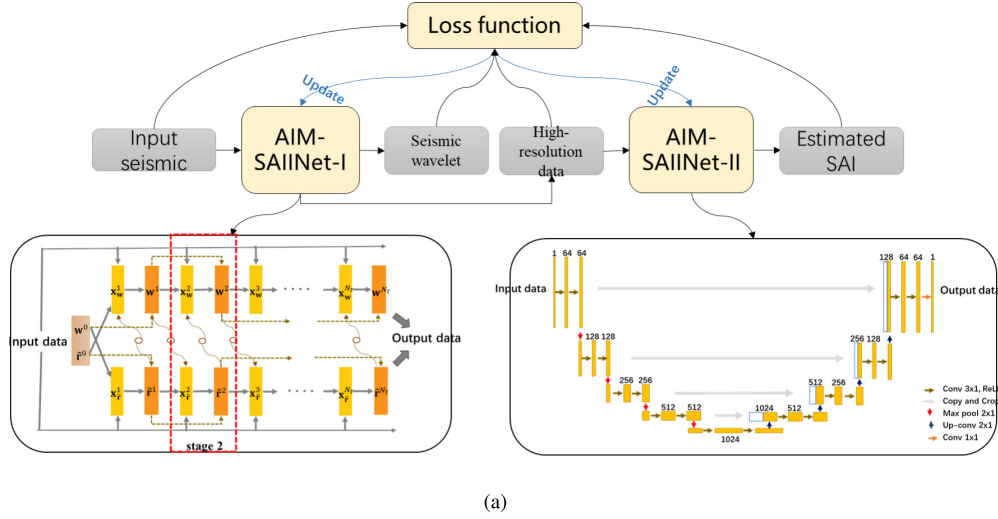


Fig. 2. Deep neural network architecture of the AIM-SAIINet. It consists of two joint network architectures, called AIM-SAIINet-I and AIM-SAIINet-II. AIM-SAIINet-I is a model-driven deep neural network and built by unrolling (9). AIM-SAIINet-II is a data-driven 1-D U-Net to map the auxiliary high-resolution data obtained from AIM-SAIINet-I into the impedance. Minimizing the loss function can update the parameters of AIM-SAIINet-I and AIM-SAIINet-II.

and joint approach. Here, we analyze these three training strategies from the perspective of semisupervised learning and then select an optimal strategy. Note that the semisupervised learning, also called semisupervised training, is implemented using the training sets with a small amount of labeled data and a large amount of unlabeled data to update the network parameters, while supervised learning only uses a large amount of labeled data to update the network parameters.

The sequential approach is a manner of two-step training strategy, i.e., the parameter  $\Theta'$  is first learned, and then, the output of AIM-SAIINet-I is input into AIM-SAIINet-II to update parameter  $\Theta''$ . The sequential approach is used to train these two tasks independently to alleviate the training burden. It is nonconvenient to adopt the semisupervised training strategy and easy to generate an intermediate loss. Different from the sequential approach, the end-to-end approach treats AIM-SAIINet as a whole. Only one-step training is required, and the intermediate variables are ignored. It means that the intermediate variables do not have a clear physical meaning, i.e., the seismic wavelet and high-resolution data cannot be estimated accurately, which fails to promote the impedance inversion. Furthermore, it is not conducive to adopting semisupervised learning because of no accurate seismic wavelet  $\mathbf{w}$ . The joint approach is a middle way of the above two approaches. In this case, parameters  $\Theta'$  and  $\Theta''$  are jointly learned. This approach is similar to the end-to-end approach to treat AIM-SAIINet as a whole, while the difference is that the intermediate variables  $\tilde{\mathbf{r}}$  and  $\mathbf{w}$  have concrete physical meanings similar to the sequential approach. It facilitates the realization of semisupervised learning, i.e., the semisupervised learning strategy can be simultaneously applied into parameters  $\Theta'$  and  $\Theta''$  to obtain an accurate impedance.

In this article, we design a semisupervised joint training strategy based on the above joint approach. The following formula shows the concrete loss function by setting loss function  $E$  as mean square error (MSE) and incorporating

data-consistent loss function:

$$\begin{aligned}
 E(\Theta) &= L_1 + L_2 + L_3 + L_4 \\
 &= \frac{1}{N} \sum_{i=1}^N \{ \|\mathcal{C}_{\Theta'}^{\dagger}(\mathbf{y}_i, \mathbf{r}_i) - \mathbf{r}_i^{gt}\|_2^2 \} \\
 &\quad + \frac{1}{N} \sum_{i=1}^N \{ \|\mathcal{T}_{\Theta}^{\dagger}(\mathbf{y}_i) - \mathbf{z}_i^{gt}\|_2^2 \} \\
 &\quad + \frac{\zeta_1}{N} \sum_{i=1}^N \{ \|\mathbf{r}_i^{gt} * \mathcal{C}_{\Theta'}^{\dagger}(\mathbf{y}_i, \mathbf{w}_i) - \mathbf{y}_i\|_2^2 \} \\
 &\quad + \frac{\zeta_2}{M} \sum_{j=1}^M \{ \|\mathbf{W} \mathbf{D} \circ \mathcal{T}_{\Theta}^{\dagger}(\mathbf{y}_j) - \mathbf{y}_j\|_2^2 \} \quad (13)
 \end{aligned}$$

where the convolution matrix  $\mathbf{W}$  consists of the estimated wavelet obtained from  $\mathcal{C}_{\Theta'}^{\dagger}$ .  $\mathbf{r}_i^{gt}$  and  $\mathbf{z}_i^{gt}$  denote the ground truth high-resolution data and impedance for the  $i$ th data pair, respectively, and  $N$  and  $M$ , respectively, denote the number of labeled and unlabeled data.  $\zeta_1$  and  $\zeta_2$  denote the weights to balance the data-consistent losses and the supervised losses, respectively. When the seismic data can be modeled by the convolution model, we set  $\zeta_1 = \zeta_2 = 1$ . However, the field data are complex and do not strictly satisfy the convolution model; therefore, we need to roughly adjust  $\zeta_1$  and  $\zeta_2$ . By minimizing (13), all the parameters in AIM-SAIINet can be learned. Before that, we use the trained parameters by the supervised joint training approach by minimizing  $L_1 + L_2 + L_3$  as the initial parameters, which can take advantages of the existing labeled data and enhance the generalization of the proposed network structure. During training, the adopted optimizer is the root mean square prop (RMSprop), and the stopping criterion is determined by tracking the training and validation errors. All source codes are implemented with TensorFlow [38] on a desktop computer with an Intel Core i7-8700 CPU and a GTX1060 GPU, and we do not use GPU acceleration for a fair comparison with nonlearning regularization.

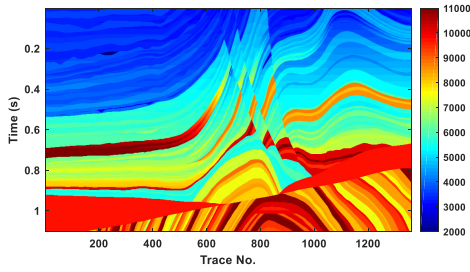


Fig. 3. Marmousi II impedance model. Traces 400–1000 of the impedance are used to generate training data to pretrain AIM-SAIINet, and the remaining data are used to generate test data.

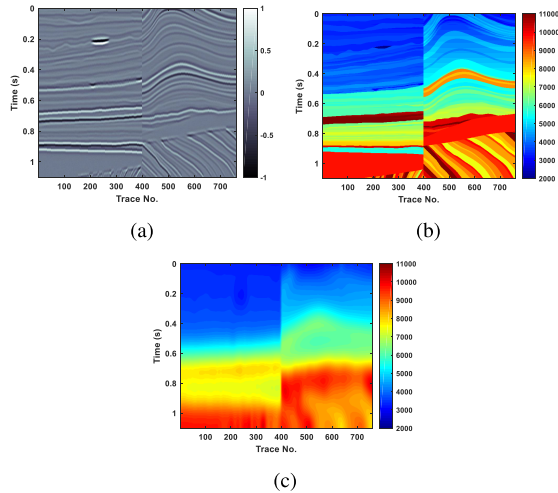


Fig. 4. Test data and impedance model. (a) Synthetic test data which is normalized. (b) Accurate acoustic impedance profile. (c) Accurate low-frequency impedance profile.

#### IV. EXAMPLES

To validate the proposed AIM-SAIINet, we use the synthetic and field data examples to show its advantages. Specifically, we first describe the generation of datasets in each example section. Then, we conduct some experiments to demonstrate the effectiveness of AIM-SAIINet.

##### A. Synthetic Data Example

1) *Datasets*: In this section, we use the Marmousi II model as a case study. We use the Marmousi II model to generate the acoustic impedance by the product of velocity and density, as shown in Fig. 3. Based on (1), we use 400–1000 traces of impedance with an interval of 2 in Fig. 3 to generate training data, and the remaining impedance on both sides is used to generate test data. Fig. 4(a) shows the synthetic test data that are generated by bringing a Ricker wavelet with 25-Hz dominant frequency and 45° rotated phase and the impedance in Fig. 4(b) into (1). Besides, we add some random noise to obtain 25-dB noisy data. For this test data, we reorder them to make the  $x$ -coordinate readable, and we treat trace-150 and trace-550 as known well logs that are used for semisupervised training. To alleviate the dependence on the deep neural network, we assume that the low-frequency impedance is known,

and here, we obtain it by filtering the accurate impedance in Fig. 4(b) with a low-pass filter with a cutoff frequency of 3 Hz, as shown in Fig. 4(c). To take advantage of the existing labeled data and reduce the training burden of semisupervised learning, we generate synthetic training datasets with given low-frequency impedance to pretrain AIM-SAIINet in a supervised manner. First, we estimate two zero-phase wavelets by spectral smoothing from the well logs in test data and give some phase shifts (0°–60° with an interval of 10°) to build a wavelet library to participate in training. Though the wavelet waveform in this wavelet library deviates from the accurate wavelet in the test data, the proposed AIM-SAIINet can obtain an accurate inversion result because of its good generalization and training strategy, as shown in Section IV-A2. The training and validation data are generated by the convolution between an arbitrary wavelet in the wavelet library and any single-trace labeled impedance (trace-400 to trace-1000) in Fig. 3 mapped by nonlinear operator  $D$ . To increase the antinoise, three levels of noise are added to training and validation data, i.e., 20-, 30-, and 50-dB noise. The number of training and validation data is 10080 and 2520, respectively. To promote the impedance inversion, we constrain the intermediate variable in loss function (13) to obtain auxiliary high-resolution data, and the labeled high-resolution data are obtained by applying the nonlinear relation  $D(z)$  to the generated impedance training data. Then, a broadband wavelet, e.g., Yu wavelet [39], is convolved with them for convenience to train.

2) *Experiments*: To validate our proposed method, we conduct some experiments in the following. First, we analyze the sensitivity of AIM-SAIINet to noise. Second, we test the effect of the given low-frequency impedance on the inversion result. Finally, we compare AIM-SAIINet with some methods to show its effectiveness. Before experiments, we first apply the above generated training data to pretrain AIM-SAIINet in a supervised manner by minimizing  $L_1 + L_2 + L_3$  in (13) to provide good initial values. Then, we apply semisupervised training to test data to tune AIM-SAIINet. The learning rates corresponding to supervised and semisupervised trainings are  $1e^{-3}$  and  $1e^{-5}$ , respectively, and the batch sizes corresponding to them are 20 and 2.

Fig. 5(a) shows the influence of different levels of noise on the inversion results using AIM-SAIINet. Here, we generate some noisy test datasets by adding 10-35-dB noise into noise-free data corresponding to that in Fig. 4(a) and use MSE to evaluate the inversion results. Before this test, we merely train AIM-SAIINet in a semisupervised training manner for different noise levels of data, and the time of each training is about 10 min. Through observation, when the signal-to-noise ratio (SNR) of the test data increases, the MSE of the inversion data decreases. Besides, if the noise levels are greater, the influence on the inversion results is greater. Especially, the inversion result of 10 dB test data corresponds to a large MSE value. Though the noise has a direct effect on the inversion results, the inversion results are acceptable, and the Pearson correlation coefficient (PCC) is higher than 0.99. Fig. 5(b) shows the effect of the given low-frequency impedance on the inversion result using AIM-SAIINet, where the test data are shown in Fig. 4(a), and the low-frequency impedance is



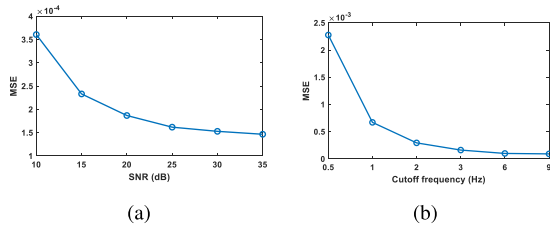


Fig. 5. (a) Influence of noise on the inversion results using AIM-SAIINet. (b) Influence of the given low-frequency impedance on the inversion results using AIM-SAIINet.

obtained by filtering the data in Fig. 4(b) with some low-pass filters whose cutoff frequencies are 0.5–9 Hz. The training strategy and the evaluation parameter are similar to the above test. It can be observed that the lack of low-frequency information leads to a significant reduction of inversion accuracy, especially in the case of 0.5-Hz cutoff frequency. Therefore, accurate low-frequency impedance can greatly increase the inversion accuracy of our proposed AIM-SAIINet.

To further highlight the advantages of our proposed AIM-SAIINet, we compare it with 2-D TV, two-step inversion, and U-Net; 2-D TV is one of the most effective inversion methods to directly estimate the impedance from the observed data, and it can obtain an inversion result with good lateral continuity. The two-step inversion is often adopted in some business softwares. Here, we apply the inversion method to implement each step where the sparse spike inversion is used to estimate a full-band reflectivity, and then, the 2-D TV is performed to invert the acoustic impedance from the estimated reflectivity. If there is no special explanation, 2-D TV indicates a direct inversion method in the following descriptions. We apply PyLops [40] to implement 2-D TV and two-step inversion because PyLops is an open-source Python library providing a flexible framework to solve linear forward and inverse problems in a fully scalable manner (from tens to millions of model parameters) without the need to store large matrices in memory. The performance of these two methods depends on the selection of some sensitive parameters, e.g., regularization parameters, and therefore, we determine them optimally by some tests. Note that the seismic wavelet is unknown for our proposed AIM-SAIINet and known for 2-D TV and two-step inversion for easy comparison. In this case, if our proposed method outperforms better than them, it shows that our method is advantageous. For U-Net, it has been used to solve seismic inversion problems successfully. Here, we pretrain it in a supervised training manner, and then, a transfer training strategy with two known well logs is adopted to tune it.

We adopt AIM-SAIINet, U-Net, 2-D TV, and two-step inversion to invert the test data in Fig. 4(a), and the inversion results are shown in Fig. 6. Through observation, our proposed method AIM-SAIINet works better, and it recovers the impedance accurately with more detailed structures, as shown in Fig. 6(a). Besides, the inversion data have good lateral continuity. Comparing with AIM-SAIINet, the result using U-Net has details loss, especially in the places indicated by black arrows, and it suffers from poor lateral continuity in the section of complex structures. Therefore, the performance

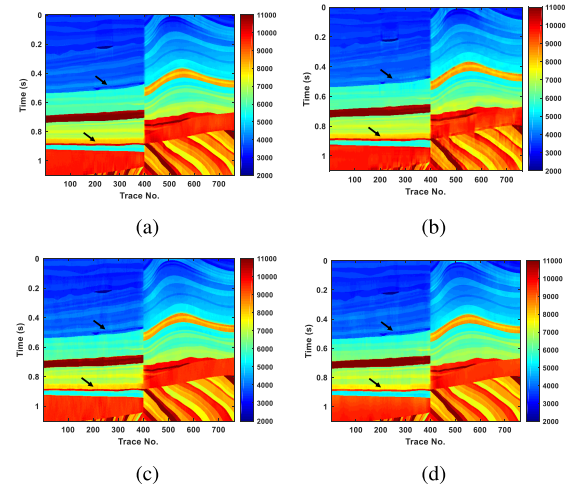


Fig. 6. Inversion results of the test data in Fig. 4(a). (a) Inversion result using AIM-SAIINet. (b) Inversion result using U-Net. (c) Inversion result using 2-D TV. (d) Inversion result using two-step inversion.

of our proposed AIM-SAIINet is better than that of U-Net. This implies that our proposed network structure and training strategy enhance the performance of U-Net, i.e., the introduced auxiliary high-resolution data promote the impedance inversion, and the estimated wavelet participates in semisupervised learning to transfer knowledge from test data. The PCCs of the estimated auxiliary high-resolution data and seismic wavelets are 0.9808 and 0.9994, respectively. The inversion results obtained by 2-D TV and two-step inversion are shown in Fig. 6(c) and (d), respectively, and they have better lateral continuity in contrast to that obtained by U-Net, and 2-D TV performs better than two-step inversion because of no intermediate loss. However, more details of these two results are lost compared with the result obtained by AIM-SAIINet, especially in the places indicated by black arrows. Therefore, our proposed AIM-SAIINet is superior to 2-D TV and two-step inversion.

For further comparison, we compute the error data by subtracting the inversion results in Fig. 6 from the accurate acoustic impedance in Fig. 4(b), as shown in Fig. 7. Through observation, the error data in Fig. 7(a) are smaller. Comparatively, the remaining error data are bigger. The error data corresponding to U-Net have obvious low-frequency trend errors because of the limited performance of U-Net, especially in the complex structures. The error data corresponding to nonlearning methods have obvious boundary errors because of the introduction of the 2-D TV constraint. Besides, there are also some obvious low-frequency trend errors. Except for the above qualitative analysis, we use four evaluation indexes, i.e., MSE, peak signal-to-noise ratio (PSNR), structural similarity (SSIM), and PCC, to quantitatively compare these four methods and record the computational time, as shown in Table I. Appendix B shows the concrete formulas of these evaluation indexes. Through observation on Table I, deep learning methods perform better and have higher computational efficiency than nonlearning methods, and AIM-SAIINet performs best with high inversion accuracy. Though U-Net

TABLE I  
COMPARISON OF THE INVERSION RESULTS ON MAMROUSI II MODEL USING DIFFERENT METHODS

	AIM-SAINet	U-Net	2D-TV	Two-step
MSE	1.6177e-4	3.7215e-4	4.2557e-4	5.7901e-4
PSNR	37.9109	34.2928	33.7103	32.3731
SSIM	0.9949	0.9888	0.9879	0.9834
PCC	0.9979	0.9953	0.9947	0.9927
Time (s/point)	4.0775e-5	3.0886e-5	3.7673e-4	1.0783e-3

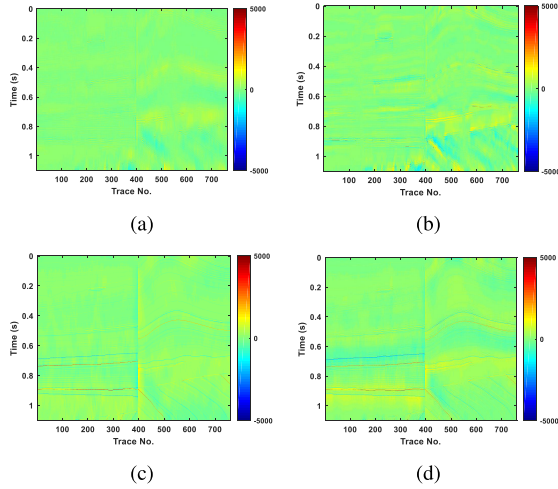


Fig. 7. Error data of the inversion results in Fig. 6. (a) Error result corresponding to Fig. 6(a). (b) Error result corresponding to Fig. 6(b). (c) Error result corresponding to Fig. 6(c). (d) Error result corresponding to Fig. 6(d).

has less computational time, the time difference between U-Net and AIM-SAINet is not so big. Based on the above analyses, our proposed method AIM-SAINet can be applied to accurately recover the acoustic impedance from synthetic data at a fast computational speed.

### B. Field Data Example

1) *Datasets and Training Strategy*: It is an effective manner to validate our proposed AIM-SAINet by a field data test. Fig. 8(a) shows the observed data with a size of  $141 \times 142$  (1-ms time sampling), and there are three known impedance well logs. To make the proposed network more credible and targeted, we use the synthetic data generated by the known well logs to pretrain AIM-SAINet. First, we interpolate the first two well logs and generate a synthetic impedance profile. Then, we estimate two seismic wavelets from the first two well logs. The training data used to pretrain AIM-SAINet can be generated by bringing synthetic impedance and any wavelet into (1), and the number is equal to 284. When training, the training batch size is set as 10. Before this training, we use the training weights obtained from the above Marmousi II model as the initial weights in this section to further reduce the training burden of AIM-SAINet. Based on the generalization of the deep neural network, we set the learning rate as 0.0005. After pretraining 1000 iterations (spending about 4 min), we train the field data in a semisupervised

fashion for 500 iterations (spending about 1.5 min, the batch size is 2, and the learning rate is 0.0001), where the first two known well logs participate in training and the last well log is used to verify. Here, we set  $\zeta_1 = 0.1$  and  $\zeta_2 = 0.01$  in (13) by some simple tests because the relation between field data and well logs does not satisfy the convolution model. If  $\zeta_1$  and  $\zeta_2$  are large, it will force the observed data and well logs to meet the convolution model, and therefore, the inversion accuracy and resolution of the acoustic impedance are reduced. Conversely, there is no data-consistent loss to constrain the seismic wavelet and adjust the low-frequency information of the inversion results.

2) *Experiments*: To validate our proposed AIM-SAINet, we adopt U-Net and 2-D TV as comparison methods. For U-Net, we pretrain it and use the first two well logs to tune the network in a transfer training manner. For 2-D TV, the seismic wavelet is estimated from the known well logs. Before inversion, we treat the low-frequency impedance background as known. Here, we filter the interpolation profile obtained by three known well logs to generate a low-frequency impedance profile, as shown in Fig. 8(b). Fig. 8(c)–(e) shows the inversion results of AIM-SAINet, U-Net, and 2-D TV methods, respectively. Fig. 8(f) shows the inverted auxiliary high-resolution result. It improves the resolution of the observed data in Fig. 8(a) and matches the validation well log (Well-3). It means that our proposed AIM-SAINet can obtain credible high-resolution data. Through observation on Fig. 8(c)–(e), it can be seen that the inversion result in Fig. 8(c) has high-resolution structures with much more details, and it has good lateral continuity. In addition, the impedance near the verification well log (Well-3) matches the trend of verification well. In comparison, the inversion result using U-Net has details loss, and the lateral continuity is not good. Though the result obtained by 2-D TV is smooth, it is difficult to invert a high-resolution impedance result using 2-D TV in practice, because of the linear assumption of the forward model and the limited performance of the constraint function. However, the inversion results using 2-D TV can recover large-scale structures well. To quantitatively compare these three methods, we record the PCC of the inversion results corresponding to the validation well log, as shown in Table II. Because we treat that the low-frequency of impedance is known, we also compute the PCC of the high-frequency impedance. Through observation, the inversion results of AIM-SAINet and U-Net match the validation well log better in contrast to 2-D TV. Besides, our proposed AIM-SAINet performs best with high PCC and recovers more details. Finally, we record the test



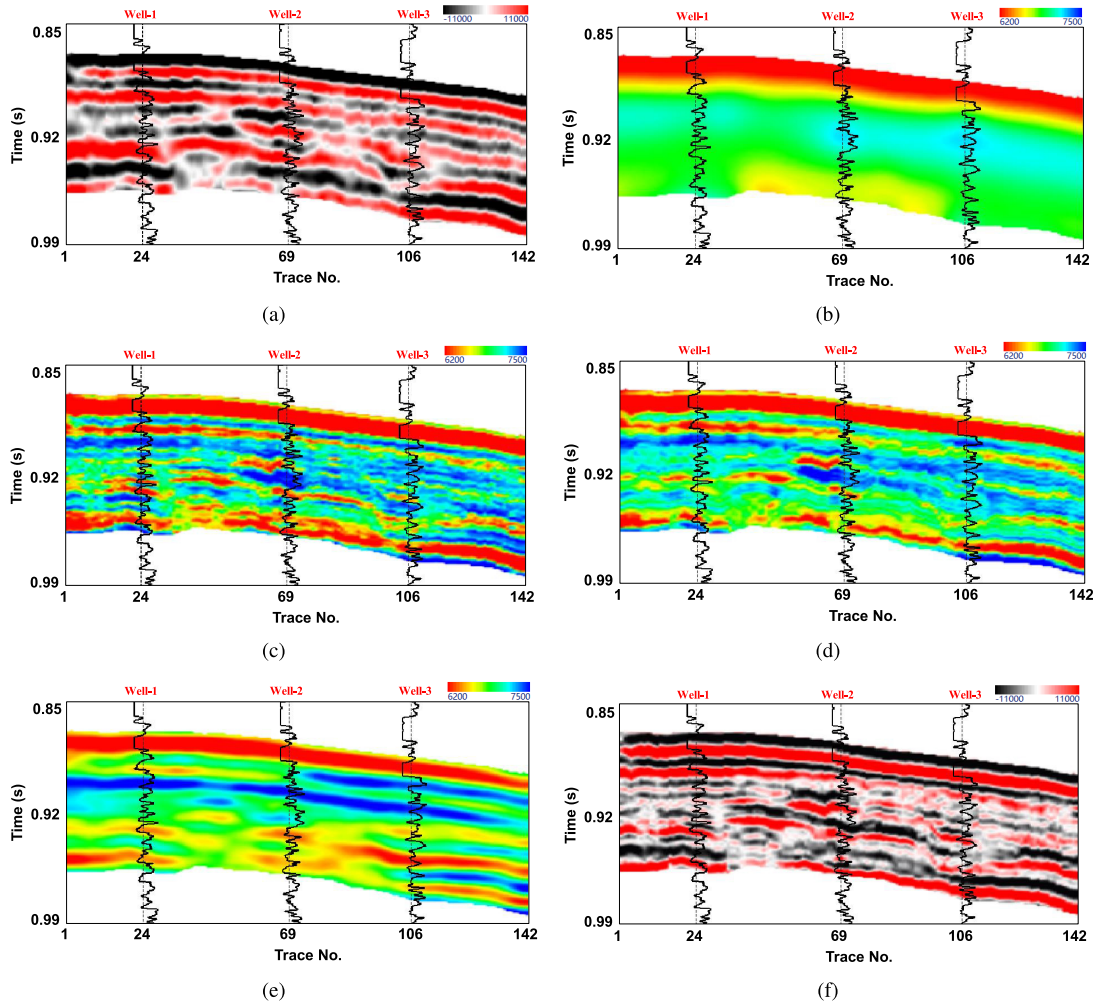


Fig. 8. Inversion results of the field data. (a) Observed post-stack data. (b) Low-frequency impedance profile. (c) Inversion result using AIM-SAIINet. (d) Inversion result using U-Net. (e) Inversion result using 2-D TV. (f) Inverted auxiliary high-resolution data using AIM-SAIINet.

TABLE II

COMPARISON OF THE INVERSION RESULTS ON FIELD DATA NEAR THE WELL-3 LOG USING DIFFERENT METHODS

	AIM-SAIINet	U-Net	2D-TV
PCC- $AI$	0.8296	0.7915	0.7108
PCC- $AI_h$	0.6383	0.6038	0.3167

time of AIM-SAIINet, U-Net, and 2-D TV, and they are, respectively, 1.7, 1.5, and 5.2 s. It can be seen that the deep learning methods have high computational efficiency in the case of not considering the training time.

Based on the above analysis, it validates that AIM-SAIINet can be used to invert credible acoustic impedance from the field data and has high computational efficiency, especially for the large data volume.

## V. CONCLUSION

We build a new deep neural network AIM-SAIINet to implement the nonlinear acoustic impedance inversion. It is designed by parameterizing the AIM and incorporating with

deep neural networks to learn the proximal operators and a nonlinear mapping. The proposed AIM-SAIINet can be split into two parts where the first part is used to learn the seismic wavelet and auxiliary high-resolution data that are treated as prior information to promote the impedance inversion, and the second part is used to learn the mapping between the inverted auxiliary high-resolution data and impedance. Different from the conventional two-step inversion, we adopt a joint training strategy, in which the supervised training is applied to pretrain AIM-SAIINet, and then, a semisupervised training is adopted to tune it, to alleviate the intermediate loss and transmit the impedance information to update the wavelet and high-resolution data. Comparing with the nonlearning regularization methods, our proposed AIM-SAIINet can mitigate the determination of sensitive parameters and constraint function, and it can improve the computational efficiency because of the incorporation with deep neural networks. Finally, we have validated the proposed AIM-SAIINet, which performs better than U-Net, 2-D TV, and two-step inversion. Therefore, our proposed method AIM-SAIINet has a great potential to widely apply to field data.

## APPENDIX A DERIVATIONS OF (9)

Here, we reviewed the derivations of (9), which represents the solutions of subproblems (7a) and (7b) in the case of  $\mu = 0$ . Here, because of the similar form of (7a) and (7b), we take problem (7a) as an example to obtain its solution by adopting the HQS algorithm. First, we introduce an auxiliary variable  $\mathbf{x}_{\tilde{\mathbf{r}}}$ , and then, (7a) is reformulated as the following Lagrangian form:

$$\min_{\tilde{\mathbf{r}}, \mathbf{x}_{\tilde{\mathbf{r}}}} \frac{1}{2} \|\mathbf{y} - \mathbf{w} * \mathbf{x}_{\tilde{\mathbf{r}}}\|_2^2 + \alpha \Lambda(\tilde{\mathbf{r}}) + \zeta_1 \|\mathbf{x}_{\tilde{\mathbf{r}}} - \tilde{\mathbf{r}}\|_2^2 \quad (14)$$

where  $\zeta_1$  denotes the penalty parameter. We split (14) into the following subproblems to solve them alternatively:

$$\mathbf{x}_{\tilde{\mathbf{r}}}^k = \arg \min_{\mathbf{x}_{\tilde{\mathbf{r}}}} \frac{1}{2} \|\mathbf{y} - \mathbf{w} * \mathbf{x}_{\tilde{\mathbf{r}}}\|_2^2 + \zeta_1 \|\mathbf{x}_{\tilde{\mathbf{r}}} - \tilde{\mathbf{r}}^{k-1}\|_2^2 \quad (15)$$

$$\tilde{\mathbf{r}}^k = \arg \min_{\tilde{\mathbf{r}}} \alpha \Lambda(\tilde{\mathbf{r}}) + \zeta_1 \|\mathbf{x}_{\tilde{\mathbf{r}}}^k - \tilde{\mathbf{r}}\|_2^2 \quad (16)$$

where  $k$  denotes the  $k$ th iteration. Equation (15) has an analytic solution obtained by making the gradient of it with respect to  $\mathbf{x}_{\tilde{\mathbf{r}}}$  zero, and it can be calculated in the frequency domain. For (16), we can write it into proximal version. Therefore, the solutions of (15) and (16) are obtained as follows:

$$\mathbf{x}_{\tilde{\mathbf{r}}}^k = \mathcal{F}^{-1} \left( \frac{[\mathcal{F}(\mathbf{w}^{k-1})]^* \odot \mathcal{F}(\mathbf{y}) + \zeta_1^k \mathcal{F}(\tilde{\mathbf{r}}^{k-1})}{[\mathcal{F}(\mathbf{w}^{k-1})]^* \odot \mathcal{F}(\mathbf{w}^{k-1}) + \zeta_1^k} \right) \quad (17)$$

$$\tilde{\mathbf{r}}^k = \text{prox}_{\zeta_1^k g}(\mathbf{x}_{\tilde{\mathbf{r}}}^k) \quad (18)$$

where  $\text{prox}_{\zeta_1^k g}$  denotes the proximal operator defined as  $\text{prox}_{\zeta_1^k g}(\mathbf{x}_{\tilde{\mathbf{r}}}^k) = \arg \min_{\tilde{\mathbf{r}}} g(\tilde{\mathbf{r}}) + \zeta_1 \|\mathbf{x}_{\tilde{\mathbf{r}}}^k - \tilde{\mathbf{r}}\|_2^2$  with  $g(\tilde{\mathbf{r}}) = \alpha \Lambda(\tilde{\mathbf{r}})$ . Similar to (7a), we can obtain the solutions of (7b), which is represented as

$$\mathbf{x}_{\tilde{\mathbf{r}}}^k = \mathcal{F}^{-1} \left( \frac{[\mathcal{F}(\tilde{\mathbf{r}}^k)]^* \odot \mathcal{F}(\mathbf{y}) + \zeta_2^k \mathcal{F}(\mathbf{w}^{k-1})}{[\mathcal{F}(\tilde{\mathbf{r}}^k)]^* \odot \mathcal{F}(\tilde{\mathbf{r}}^k) + \zeta_2^k} \right) \quad (19)$$

$$\mathbf{w}^k = \text{prox}_{\zeta_2^k f}(\mathbf{x}_{\tilde{\mathbf{r}}}^k) \quad (20)$$

where  $\text{prox}_{\zeta_2^k f}$  denotes the proximal operator defined as  $\text{prox}_{\zeta_2^k f}(\mathbf{x}_{\tilde{\mathbf{r}}}^k) = \arg \min_{\mathbf{w}} f(\mathbf{w}) + \zeta_2 \|\mathbf{x}_{\tilde{\mathbf{r}}}^k - \mathbf{w}\|_2^2$  with  $f(\mathbf{w}) = \beta \Phi(\mathbf{w})$ . According to (17)–(20), we can obtain (9).

## APPENDIX B EQUATIONS OF FOUR EVALUATION INDEXES

During experiments, we used MSE, PSNR, SSIM, and PCC to evaluate the performance of our proposed method. Here, we list the equations of these four evaluation indexes as follows:

$$\text{MSE} = \frac{1}{N \times M} \sum_{i=1}^M \sum_{j=1}^N (f^{gt}(i, j) - f(i, j))^2 \quad (21)$$

$$\text{PSNR} = 10 \log_{10} \frac{Q^2}{\text{MSE}} \quad (22)$$

$$\text{SSIM} = \frac{(2\mu_{\mathbf{f}^{gt}}\mu_{\mathbf{f}} + c_1)(\sigma_{\mathbf{f}^{gt}\mathbf{f}}^2 + c_2)}{(\mu_{\mathbf{f}^{gt}}^2 + \mu_{\mathbf{f}}^2 + c_1)(\sigma_{\mathbf{f}^{gt}}^2 + \sigma_{\mathbf{f}}^2 + c_2)} \quad (23)$$

$$\text{PCC} = \frac{\sum_{i=1}^{N \times M} (x^{gt}(i) - \mu_{\mathbf{x}^{gt}})(x(i) - \mu_{\mathbf{x}})}{\sqrt{\sum_{i=1}^{N \times M} (x^{gt}(i) - \mu_{\mathbf{x}^{gt}})^2 \sum_{i=1}^{N \times M} (x(i) - \mu_{\mathbf{x}})^2}} \quad (24)$$

where  $f^{gt}(i, j)$  and  $f(i, j)$  denote the  $(i, j)$ th point of the ground truth data and inverted data, respectively.  $N$  and  $M$  represent the trace number and time sampling point number, respectively.  $Q$  indicates the maximum pixel value.  $\mathbf{f}^{gt}$  and  $\mathbf{f}$  denote the matrix forms corresponding to  $f^{gt}(i, j)$  and  $f(i, j)$ , respectively.  $\mathbf{x}^{gt}$  and  $\mathbf{x}$  are generated by vectorizing  $\mathbf{f}^{gt}$  and  $\mathbf{f}$ , respectively, and the  $i$ th points of them are represented as  $x^{gt}(i)$  and  $x(i)$ .  $c_1$  and  $c_2$  are constants for avoiding instability.  $\mu_{\bullet}$  and  $\sigma_{\bullet}$ , respectively, denote the mean and standard deviation of  $\bullet$ , respectively, and  $\sigma_{\bullet\star}$  denotes the covariance between  $\bullet$  and  $\star$ .

## ACKNOWLEDGMENT

The authors would like to thank BGP Inc., China National Petroleum Corporation, for providing the field data and Z. Q. Wang for useful discussions. Hongling Chen would like to thank S. A. Shen for his support.

## REFERENCES

- [1] R. B. Latimer, R. Davidson, and P. van Riel, "An interpreter's guide to understanding and working with seismic-derived acoustic impedance data," *Lead. Edge*, vol. 19, no. 3, pp. 242–256, Mar. 2000.
- [2] Z. Xu and J. Sun, "Model-driven deep-learning," *Nat. Sci. Rev.*, vol. 5, no. 1, pp. 22–24, Jan. 2017.
- [3] R. Zhang and J. Castagna, "Seismic sparse-layer reflectivity inversion using basis pursuit decomposition," *Geophysics*, vol. 76, no. 6, pp. R147–R158, Nov. 2011.
- [4] A. Gholami, "Nonlinear multichannel impedance inversion by total-variation regularization," *Geophysics*, vol. 80, no. 5, pp. R217–R224, Sep. 2015.
- [5] M. D. Sacchi, "Reweight strategies in seismic deconvolution," *Geophys. J. Int.*, vol. 129, no. 3, pp. 651–656, Jun. 1997.
- [6] D. R. Velis, "Stochastic sparse-spike deconvolution," *Geophysics*, vol. 73, no. 1, pp. R1–R9, Jan. 2008.
- [7] A. Gholami and M. D. Sacchi, "A fast and automatic sparse deconvolution in the presence of outliers," *IEEE Trans. Geosci. Remote Sens.*, vol. 50, no. 10, pp. 4105–4116, Oct. 2012.
- [8] X. Xu, J. Gao, B. Zhang, H. Chen, and Y. Yang, "Multichannel reflectivity inversion with sparse group regularization based on HPPSG algorithm," *IEEE Geosci. Remote Sens. Lett.*, vol. 17, no. 5, pp. 784–788, May 2020.
- [9] A. Gholami and M. D. Sacchi, "Fast 3D blind seismic deconvolution via constrained total variation and GCV," *SIAM J. Imag. Sci.*, vol. 6, no. 4, pp. 2350–2369, 2013.
- [10] L. Wang, Q. Zhao, J. Gao, Z. Xu, M. Fehler, and X. Jiang, "Seismic sparse-spike deconvolution via toeplitz-sparse matrix factorization," *Geophysics*, vol. 81, no. 3, pp. V169–V182, May 2016.
- [11] H. Chen, J. Gao, N. Liu, and Y. Yang, "Multitrace semiblind nonstationary deconvolution," *IEEE Geosci. Remote Sens. Lett.*, vol. 16, no. 8, pp. 1195–1199, Aug. 2019.
- [12] Y. Sui and J. Ma, "Blind sparse-spike deconvolution with thin layers and structure," *Geophysics*, vol. 85, no. 6, pp. V481–V496, Nov. 2020.
- [13] D. W. Oldenburg, T. Scheuer, and S. Levy, "Recovery of the acoustic impedance from reflection seismograms," *Geophysics*, vol. 48, no. 10, pp. 1318–1337, Oct. 1983.
- [14] C. Walker and T. J. Ulrych, "Autoregressive recovery of the acoustic impedance," *Geophysics*, vol. 48, no. 10, pp. 1338–1350, Oct. 1983.
- [15] B. H. Russell, *Recursive Inversion—Theory*, 2012, ch. 3, pp. 3–1–3–9.
- [16] H. Hamid and A. Pidlisecky, "Multitrace impedance inversion with lateral constraints," *Geophysics*, vol. 80, no. 6, pp. M101–M111, Nov. 2015.
- [17] S. Yuan, S. Wang, C. Luo, and Y. He, "Simultaneous multitrace impedance inversion with transform-domain sparsity promotion," *Geophysics*, vol. 80, no. 2, pp. R71–R80, Mar. 2015.
- [18] A. Gholami, "A fast automatic multichannel blind seismic inversion for high-resolution impedance recovery," *Geophysics*, vol. 81, no. 5, pp. V357–V364, Sep. 2016.
- [19] D. A. Cooke and W. A. Schneider, "Generalized linear inversion of reflection seismic data," *Geophysics*, vol. 48, no. 6, pp. 665–676, 1983.

- [20] Z. Wang, J. Gao, H. Zhao, B. Zhang, and Z. Gao, "A new approach for blind nonlinear acoustic impedance inversion," *IEEE Geosci. Remote Sens. Lett.*, early access, Feb. 3, 2021, doi: [10.1109/LGRS.2020.3047495](https://doi.org/10.1109/LGRS.2020.3047495).
- [21] X. Ma, "A constrained global inversion method using an overparameterized scheme: Application to poststack seismic data," *Geophysics*, vol. 66, no. 2, pp. 613–626, Mar. 2001.
- [22] Z. Gao, Z. Pan, and J. Gao, "Multimutation differential evolution algorithm and its application to seismic inversion," *IEEE Trans. Geosci. Remote Sens.*, vol. 54, no. 6, pp. 3626–3636, Jun. 2016.
- [23] X. Wu, L. Liang, Y. Shi, and S. Fomel, "FaultSeg3D: Using synthetic data sets to train an end-to-end convolutional neural network for 3D seismic fault segmentation," *Geophysics*, vol. 84, no. 3, pp. IM35–IM45, May 2019.
- [24] N. Liu, T. He, Y. Tian, B. Wu, J. Gao, and Z. Xu, "Common-azimuth seismic data fault analysis using residual UNet," *Interpretation*, vol. 8, no. 3, pp. SM25–SM37, Aug. 2020.
- [25] S. Yu, J. Ma, and W. Wang, "Deep learning for denoising," *Geophysics*, vol. 84, no. 6, pp. V333–V350, Nov. 2019.
- [26] F. Yang and J. Ma, "Deep-learning inversion: A next-generation seismic velocity model building method," *Geophysics*, vol. 84, no. 4, pp. R583–R599, Jul. 2019.
- [27] B. Wu, D. Meng, L. Wang, N. Liu, and Y. Wang, "Seismic impedance inversion using fully convolutional residual network and transfer learning," *IEEE Geosci. Remote Sens. Lett.*, vol. 17, no. 12, pp. 2140–2144, Dec. 2020.
- [28] V. Das, A. Pollack, U. Wollner, and T. Mukerji, "Convolutional neural network for seismic impedance inversion," *Geophysics*, vol. 84, no. 6, pp. R869–R880, Nov. 2019.
- [29] Y. Wang, Q. Ge, W. Lu, and X. Yan, "Well-logging constrained seismic inversion based on closed-loop convolutional neural network," *IEEE Trans. Geosci. Remote Sens.*, vol. 58, no. 6, pp. 5564–5574, Aug. 2020.
- [30] R. Biswas, M. K. Sen, V. Das, and T. Mukerji, "Prestack and post-stack inversion using a physics-guided convolutional neural network," *Interpretation*, vol. 7, no. 3, pp. SE161–SE174, Aug. 2019.
- [31] M. Alfarraj and G. AlRegib, "Semisupervised sequence modeling for elastic impedance inversion," *Interpretation*, vol. 7, no. 3, pp. SE237–SE249, Aug. 2019.
- [32] W. Zhang, J. Gao, Z. Gao, and H. Chen, "Adjoint-driven deep-learning seismic full-waveform inversion," *IEEE Trans. Geosci. Remote Sens.*, early access, Dec. 29, 2021, doi: [10.1109/TGRS.2020.3044065](https://doi.org/10.1109/TGRS.2020.3044065).
- [33] H. Chen, J. Gao, X. Jiang, Z. Gao, and W. Zhang, "Optimization-inspired deep learning high-resolution inversion for seismic data," *Geophysics*, vol. 86, no. 3, pp. R265–R276, May 2021.
- [34] N. Wang and J. Sun, "Model meets deep learning in image inverse problems," *CSIAM Trans. Appl. Math.*, vol. 1, no. 3, pp. 365–386, 2020.
- [35] Z. Gao, J. Gao, Z. Pan, and X. Zhang, "Building an initial model for full waveform inversion using a global optimization scheme," in *Proc. SEG Tech. Program Expanded Abstr.*, 2014, pp. 1136–1141.
- [36] S. Yuan, S. Wang, Y. Luo, W. Wei, and G. Wang, "Impedance inversion by using the low-frequency full-waveform inversion result as an *a priori* model," *Geophysics*, vol. 84, no. 2, pp. R149–R164, Mar. 2019.
- [37] O. Ronneberger, P. Fischer, and T. Brox, "U-Net: Convolutional networks for biomedical image segmentation," in *Medical Image Computing and Computer-Assisted Intervention—MICCAI*, vol. 9351. Cham, Switzerland: Springer, 2015, pp. 234–241. [Online]. Available: <http://lmb.informatik.uni-freiburg.de/Publications/2015/RFB15a>
- [38] M. Abadi *et al.*, "TensorFlow: A system for large-scale machine learning," in *Proc. 12th USENIX Symp. Operating Syst. Design Implement. (OSDI)*, 2016, pp. 265–283.
- [39] S. Yu, "Wide-band ricker wavelet," *Oil Geophys. Prospecting*, vol. 31, no. 5, pp. 605–615, May 1996.
- [40] M. Ravasi and I. Vasconcelos, "PyLops—A linear-operator Python library for scalable algebra and optimization," *SoftwareX*, vol. 11, Jun. 2020, Art. no. 100361.



**Hongling Chen** received the B.S. degree in solid geophysics from Northeast Petroleum University, Daqing, China, in 2015, and the M.S. degree in geological resources and geological engineering from China University of Petroleum, Beijing, China, in 2018. She is currently pursuing the Ph.D. degree in information and communication engineering with the School of Information and Communications Engineering, Xi'an Jiaotong University, Xi'an, China.

Her research interests include seismic high-resolution inversion, seismic signal processing, and deep learning.



**Jinghuai Gao** received the M.S. degree in applied geophysics from Chang'an University, Xi'an, China, in 1991, and the Ph.D. degree in electromagnetic field and microwave technology from Xi'an Jiaotong University, Xi'an, in 1997.

From 1997 to 2000, he was a Post-Doctoral Researcher with the Institute of Geology and Geophysics, Chinese Academy of Sciences, Beijing, China. In 1999, he was a Visiting Scientist with the Modelling and Imaging Laboratory, University of California at Santa Cruz, Santa Cruz, CA, USA.

He is currently an Associate Director with the National Engineering Laboratory for Offshore Oil Exploration, Xi'an Jiaotong University. He is also a Professor with the School of Electronic and Information Engineering and the School of Mathematics and Statistics, Xi'an Jiaotong University. He is the Project Leader of the Fundamental Theory and Method for Geophysical Exploration and Development of Unconventional Oil and Gas, Xi'an Jiaotong University, which is a major program of the National Natural Science Foundation of China under Grant 41390454. His research interests include seismic wave propagation and imaging theory, seismic reservoir and fluid identification, and seismic inverse problem theory and method.

Dr. Gao was a recipient of the Chen Zongqi Geophysical Best Paper Award in 2013. He is an Editorial Board Member of the *Chinese Journal of Geophysics*, *Applied Geophysics*, and *Chinese Science Bulletin*.



**Wei Zhang** received the B.S. and M.S. degrees in solid geophysics from Northeast Petroleum University, Daqing, China, in 2015 and 2018, respectively. He is currently pursuing the Ph.D. degree in information and communication engineering with the School of Information and Communications Engineering, Xi'an Jiaotong University, Xi'an, China.

His research interests include wave equation-based imaging, inversion, and deep learning application.



**Ping Yang** received the Ph.D. degree in geophysics from China University of Petroleum, Beijing, China, in 2014.

He is currently a Senior Expert with BGP Inc., China National Petroleum Corporation, Zhuozhou, China. He has worked on deeply buried heterogeneous carbonate reservoirs of China for many years. He is now focusing on applying deep learning into seismic data processing and interpretation.